Evaluation of Precipitation Detection over Various Surfaces from Passive Microwave Imagers and Sounders

S. Joseph Munchak[1a,b], Gail Skofronick-Jackson[a]

[a]*Mesoscale Atmospheric Processes Laboratory, Code 612, NASA Goddard Space Flight Center, 8800 Greenbelt Rd., Greenbelt, MD, USA 20771*
[b]*Earth System Science Interdisciplinary Center, University of Maryland, College Park, MD, USA*

Abstract

During the middle part of this decade a wide variety of passive microwave imagers and sounders will be unified in the Global Precipitation Measurement (GPM) mission to provide a common basis for frequent (3 hr), global precipitation monitoring. The ability of these sensors to detect precipitation by discerning it from non-precipitating background depends upon the channels available and characteristics of the surface and atmosphere. This study quantifies the minimum detectable precipitation rate and fraction of precipitation detected for four representative instruments (TMI, GMI, AMSU-A, and AMSU-B) that will be part of the GPM constellation. Observations for these instruments were constructed from equivalent channels on the SSMIS instrument on DMSP satellites F16 and F17 and matched to precipitation data from NOAA's National Mosaic and QPE (NMQ) during 2009 over the continuous United States. A variational optimal estimation retrieval of non-precipitation surface and atmosphere parameters was used to determine the consistency between the observed brightness temperatures and these parameters, with high cost function values shown to be related to precipitation.

The minimum detectable precipitation rate, defined as the lowest rate for which probability of detection exceeds 50%, and the detected fraction of pre-

[1]corresponding author email: s.j.munchak@nasa.gov; ph: 1-301-286-2392; fax: 1-301-614-5492

cipitation, are reported for each sensor, surface type (ocean, coast, bare land, snow cover) and precipitation type (rain, mix, snow). The best sensors over ocean and bare land were GMI (0.22 mm hr^{-1} minimum threshold and 90% of precipitation detected) and AMSU (0.26 mm hr^{-1} minimum threshold and 81% of precipitation detected), respectively. Over coasts (0.74 mm hr^{-1} threshold and 12% detected) and snow-covered surfaces (0.44 mm hr^{-1} threshold and 23% detected), AMSU again performed best but with much lower detection skill, whereas TMI had no skill over these surfaces. The sounders (particularly over water) benefited from the use of re-analyis data (vs. climatology) to set the a-priori atmospheric state and all instruments benefit from the use of a conditional snow cover emissivity database over land. It is recommended that real-time sources of these data be used in the operational GPM precipitation algorithms.

Keywords: passive microwave, precipitation, detection, imager, sounder, emissivity, variational retrieval

---

1. Introduction

Passive microwave remote sensing of precipitation from space has advanced tremendously in the past three decades with regard to both number and capabilities of instruments in operation. The "golden age" of passive microwave precipitation is anticipated to begin in 2014 with the launch of the Global Precipitation Measurement (GPM) core satellite on a mission to unify precipitation estimates from a constellation of sensors.

Early systems such as the Electrically Scanned Microwave Radiometer (ESMR; Allison et al. (1974)) and Scanning Multi-channel Microwave Radiometer (SMMR; Gloersen and Hardis (1978)) and corresponding retrieval algorithms (*e.g.*, Wilheit et al. (1977); Prabhakara et al. (1986)) primarily focused on the retrieval of rainfall over oceans due to the clear contrast between the radiometrically cold background of the low-emissivity ocean surface and radiometrically warm emission from falling rain at low frequencies (below 50 GHz). The introduction

of the Special Sensor Microwave/Imager (SSM/I; Hollinger et al. (1990)), with vertically and horizontally polarized channels at 89 GHz in addition to the lower frequencies on SMMR allowed for detection of precipitation with the detection of brightness temperature (Tb) depressions due to the scattering produced by large, precipitation sized ice particles (*e.g.*, Wu and Weinman (1984); Spencer (1986)). Although the relationship between the amount of ice scattering and surface precipitation rate is dependent on the vertical structure of the precipitation profile (Kummerow and Weinman, 1988) and ice microphysics (Petty and Huang, 2010), it has nevertheless remained the primary source of information regarding precipitation over land surfaces due to their high, variable, and inhomogeneous emissivity.

While these instruments and algorithms generally perform well for moderate to heavy rainfall during the warm season (Ebert et al., 2007), cold-season precipitation, i.e., light rain and snowfall in particular, remains challenging (Iturbide-Sanchez et al., 2011) due to the weaker scattering signal and higher contribution from the earth surface (Skofronick-Jackson and Johnson, 2011), the emissivity of which may be complicated by the presence of snow or ice on the ground (Hewison and English, 1999). Frequencies higher than 100 GHz are particularly useful for falling snow because of increasingly effective scattering with frequency and reduced opacity of the atmosphere from water vapor in cold and dry environments (Bennartz and Bauer, 2003). An early attempt to retrieve falling snow (Liu and Curry, 1997) used the 92 and 150 GHz channels on the Special Sensor Microwave/Temperature-2 (SSM/T2) sounder in combination with temperature profiles from the ECMWF forecast model to detect snowfall over the north Atlantic using empirically-determined Tb thresholds. Empirical methods have since expanded to use the water vapor channels on Advanced Microwave Sounding Unit-B (AMSU-B) and Microwave Humidity Sounder (MHS) instruments to effectively mask the surface (Chen and Staelin (2003); Kongoli et al. (2003); Surussavadee and Staelin (2009)), improving detection skill. These algorithms generally use brightness temperature thresholds to detect precipitation and empirical regression or neural networks to determine intensity within the

3

precipitation mask.

Physically-based methods, in contrast, use radiative transfer models to simulate brightness temperatures (Tbs) from Bayesian databases of observed (Noh et al. (2006, 2009); Kummerow et al. (2011)) and modeled (Skofronick-Jackson et al. (2004); Kim et al. (2008)), or variationally-adjusted (Bauer et al. (2005); Boukabara et al. (2011)) precipitation profiles. These methods ensure physical consistency between observed Tbs and retrieved precipitation, but require accurate models of ice particle scattering (*e.g.*, Liu (2004); Kim (2006); Kim et al. (2007); Petty and Huang (2010)) and emissivity of snow and ice-covered surfaces (e.g., Hewison and English (1999); Weng et al. (2001)), which are not as mature as their counterparts regarding liquid precipitation and ocean surfaces.

The purpose of this study is to establish the minimum precipitation rate that can be reliably detected over various surface types and with various channel combinations that will be available on satellites in the GPM constellation. Because the Bayesian retrieval databases for GPM are still under development, we instead employ a variational approach that combines physical and empirical models, described in section 2 to identify precipitation using a null hypothesis test. The Special Sensor Microwave Imager/Sounder (SSMIS) is used as a proxy for various GPM-era sensors and evaluated over the continental United States using the National Mosaic and Quantitative Precipitation Estimates (NMQ; Zhang et al. (2011)). These datasets are also described in section 2 and results given in section 3. A summary and concluding remarks are given in section 4.

2. Method

This section describes the retrieval theory and dataset-specific implementation details used to delineate precipitation in this study. An example retrieval is also provided to familiarize the reader with the output of the optimal estimation method applied to this remote sensing problem.

2.1. General Retrieval Theory

A variational (optimal estimation; Rodgers (2000)) retrieval of non-precipitation surface and atmospheric parameters via the inversion of a non-scattering radiative transfer model (Elsaesser and Kummerow, 2008) has been adapted for the datasets used in this study. Essentially, we test a null hypothesis that an observed set of brightness temperatures $\mathbf{y}$ is consistent with a reasonable set of surface and clear-air atmospheric parameters $\mathbf{x}$ not including liquid or frozen precipitation. This screening method is conceptually identical to that of Bytheway and Kummerow (2010) and Boukabara et al. (2011) as well as earlier versions of the Bayesian GPROF algorithm (Kummerow et al., 2001) (more recent versions (Kummerow et al., 2011) include non-precipitating profiles in the Bayesian database, eliminating the need for an explicit screening step).

The retrieval minimizes a cost function:

$$\Phi = (\mathbf{x} - \mathbf{x}_\mathrm{a})^\mathrm{T}\mathbf{S}_\mathrm{a}^{-1}(\mathbf{x} - \mathbf{x}_\mathrm{a}) + (\mathbf{y} - f(\mathbf{x}))^\mathrm{T}\mathbf{S}_\mathrm{y}^{-1}(\mathbf{y} - f(\mathbf{x})), \tag{1}$$

where $\mathbf{x}_\mathrm{a}$ is the a-priori state vector, $\mathbf{S}_\mathrm{a}$ is the state covariance matrix, f is the forward (radiative transfer) model, and $\mathbf{S}_\mathrm{y}$ is the observation covariance matrix. The contents and formulation of $\mathbf{y}$, $\mathbf{x}_\mathrm{a}$, f, $\mathbf{S}_\mathrm{a}$, and $\mathbf{S}_\mathrm{y}$ depends on the input and ancillary datasets; further details are provided in section 2.2. Common aspects of all retrievals are the use of Rosenkrantz (1998) and Rosenkrantz (1999) for absorption of atmospheric gases (with improvements (Tretyakov et al., 2003) to the water vapor lines at 22 and 183 GHz) and the use of FASTEM4 (Liu et al., 2011) for emissivity over water surfaces.

The cost function (1) is minimized iteratively, starting from $\mathbf{x}_\mathrm{a}$, using the Gauss-Newton method to find the value of $\mathbf{x}$ where the gradient of Φ with respect to $\mathbf{x}$ is zero. This requires the calculation of the Jacobian matrix $\mathbf{K}$ at each iterative step n by calculating the derivative of each observation (y_i) with respect to each state element (x_j):

$$K_{ij} = \frac{\partial y_i}{\partial x_j}. \tag{2}$$

Before the iteration begins, $\mathbf{S}_{\mathrm{a}}$ is orthogonalized, and the variables in $\mathbf{x}$ are transformed into the corresponding EOF space. This step has two consequences which are beneficial from a computational point of view. First, $\mathbf{S}_{\mathrm{a}}$ becomes diagonal, which reduces numerical instabilities resulting from floating-point representation of ill-conditioned matrices. Second, by discarding those EOFs that represent variability below the noise level of the sensor plus approximations made in the radiative transfer model, the retrieval parameter space can be reduced, saving computation time. The iterative step is defined as:

$$\mathbf{x}_{n+1} = \mathbf{x}_n + \Delta_{\mathrm{x}} \left(\mathbf{K}_n^{\mathrm{T}} \mathbf{S}_{\mathrm{y}}^{-1} \mathbf{K}_n + \mathbf{S}_{\mathrm{y}}^{-1} \right)^{-1} \times$$
$$\left(\mathbf{K}_n^{\mathrm{T}} \mathbf{S}_{\mathrm{y}}^{-1} [\mathbf{y} - f(\mathbf{x}_n)] - \mathbf{S}_{\mathrm{a}}^{-1} [\mathbf{x}_n - \mathbf{x}_{\mathrm{a}}] \right), \tag{3}$$

where Δ_{x} is a positive value less than one (0.75 is used in this study) that guards against non-convergent oscillations about the solution, albeit at the expense of increased iterations. The iteration proceeds until a convergence criterion is satisfied. The convergence criterion we use requires that the difference between consecutive iterations is less than 10% of the retrieved state error covariance, $\mathbf{S}_{\mathrm{x}}$:

$$(\mathbf{x}_{n+1} - \mathbf{x}_n)^{\mathrm{T}} \mathbf{S}_{\mathrm{x}}^{-1} (\mathbf{x}_{n+1} - \mathbf{x}_n) < 0.1, \tag{4}$$

where $\mathbf{S}_{\mathrm{x}}$ is:

$$\mathbf{S}_{\mathrm{x}} = (\mathbf{K}^{\mathrm{T}} \mathbf{S}_{\mathrm{y}}^{-1} \mathbf{K} + \mathbf{S}_{\mathrm{a}}^{-1})^{-1}. \tag{5}$$

This is the same convergence test used by Elsaesser and Kummerow (2008); other criteria, such as

$$\frac{1}{N_{\mathrm{obs}}} \left(\mathbf{y} - f(\mathbf{x}_n) \right)^{\mathrm{T}} \mathbf{S}_{\mathrm{y}}^{-1} \left(\mathbf{y} - f(\mathbf{x}_n) \right) \leq 1, \tag{6}$$

which guarantees that the retrieved state simulate the observed Tbs within the error tolerance specified by $\mathbf{S}_{\mathrm{y}}$ (Boukabara et al., 2011), have also been used in the context of variational retrievals. Without the use of a scattering radiative transfer model, such a criterion would lead to non-convergence in many scenes, whether due to precipitation or a poor characterization of the surface/atmosphere state and covariance by $\mathbf{x}_{\mathrm{a}}$ and $\mathbf{S}_{\mathrm{a}}$. While non-convergence

6

itself has been used to identify precipitation (e.g, Elsaesser and Kummerow (2008); Bytheway and Kummerow (2010); Boukabara et al. (2011)) in this manner, for this study we are more interested in identifying the minimum threshold of Φ at which the error due to precipitation exceeds the background "noise" resulting from surface and atmospheric characterization errors in $\mathbf{x}_a$ and $\mathbf{S}_a$. Therefore it is important to find the minimum of Φ which is not guaranteed by using Eq. 6, whereas using Eq. (4) will get within 10% of the local minimum, which is likely to be the global minimum as well for the moderately non-linear radiative transfer under consideration.

2.2. Datasets

During 2009, data from the SSMIS sensor was available from the Defense Meteorological Satellite Program (DMSP) F16 and F17 satellites. SSMIS is a conically-scanning microwave radiometer that combines the imaging and sounding channels on the SSM/I, SSM/T1, and SSM/T2 instruments. At a nominal altitude of 848 km, the ground footprint ranges from 14x13 km at 183 GHz to 73x47 km at 19 GHz and the earth incidence angle is 53.1°. With 24 channels ranging from 19 to 183 GHz, SSMIS is capable of providing proxy datasets for the TRMM Microwave Imager (TMI)[2], GPM Microwave Imager (GMI), and the AMSU/MHS sounders (SNDA/SNDB) that will form the GPM constellation. These proxy datasets mimic the frequency and polarization combinations on these sensors with the exception of the horizontally and vertically-polarized 10-GHz channels on TMI and GMI and the vertically-polarized 166 GHz channel on GMI. The cross-track scan geometry of the AMSU sensors cannot be replicated, which places the weighting functions of the water vapor (177-189 GHz) and temperature (50-60 GHz) sounding channels somewhat higher in the atmosphere than AMSU, depending on scan position. The channels used in each

---

[2]The Advanced Microwave Scanning Radiometer 2 (AMSR2), launched in May 2012 and also expected to be part of the GPM constellation, has similar channels to its predecessor, AMSR-E.

of these proxy datasets are given in Table 1. Note that for SNDA (AMSU-A+B proxy) only the first three 50-GHz temperature sounding channels, with weighting functions primarily in the troposphere, were included, since the remaining temperature sounding channels are not expected to be sensitive to precipitation.

[Table 1 about here.]

The source of data was the Temperature Data Record (TDR) maintained by NOAA[3]. This record applies corrections (Yan and Weng, 2008) to known calibration problems related to warm load solar intrusions and an emissive antenna on the F16 sensor (Kunkee et al., 2008) (the latter of these is also present, to a lesser extent, on F17). Each TDR was manually examined for visually obvious calibration artifacts. If any artifacts were present (most commonly in the 91H channel on F16 due to warm load solar intrusions), the file was removed from the analysis. To accommodate remaining uncertainties in the sensor calibration and forward model approximations, the diagonal elements of S_y are set to $(3 K)^2$ with zero covariance assumed.

The TDR provides imager (91-183 GHz), environmental (19-37 GHz) and sounding (50-60 GHZ) channels with 1x1, 2x1, and 3x3 cross-track by along-track sample averaging, respectively. For this study, all of the proxy sensor datasets were commonly gridded at one-half (2x2) the native SSMIS sample resolution, providing a cross-track and along-track spacing of 25 km. This required spatially averaging the imager channels and linearly interpolating the sounding channels. The SNDB dataset was also retained at native resolution because it consists solely of a subset of the high-resolution imager channels.

The datasets used to validate the detection of precipitation come from the National Mosaic and Quantitative Precipitation Estimate (NMQ; Zhang et al. (2011)) suite of products. These include three-dimensional reflectivity and a

---

[3]At the time of publication, intercalibrated SSMIS data were available at http://mrain.atmos.colostate.edu/LEVEL1C/ created with the method of (Sapiano et al., 2012). Because the reference sensor is TMI, the intercalibration is applied only to the 19, 22, 37, and 91 GHz channels on SSMIS.

number of radar-only and gauge-adjusted precipitation rate estimates. These are available every 5 minutes at 0.01° resolution. For our validation, we used the radar-only Q2 product. This product is based on the mosaic of hybrid scan reflectivity, which is a composite of the lowest elevation angle quality-controlled reflectivity from the National Weather Service WSR-88D Crum and Alberty (1993) and Environment Canada C-band radar networks. Precipitation is classified as convective, stratiform, warm rain, hail, or snow based on radar profile characteristics and ancillary temperature and humidity data, then a corresponding Z-R relationship is applied to derive the precipitation rate. The advantage of the NMQ-Q2 product is in the high spatial and temporal resolution, but as with any ground-based radar product, shallow precipitation may be missed due to beam elevation and terrain blockage (Maddox et al., 2002). In addition, errors in rain type classification or variability of the Z-R relationship within a class, as well as the increasing distance between the surface and the radar beam with distance from the transmitter, are sources of error in cases when an echo is detected that must be considered when using the rain rate data. To alleviate the beam elevation-induced error, areas with a beam elevation greater than 1.5 km above the ground were excluded from the analysis.

The radar-only Q2 data were matched to each SSMIS footprint using a weighting function designed to mimic the SSMIS antenna pattern, without requiring satellite navigation information. A two-dimensional symmetric Gaussian weighting function with a half-power beamwidth of 38 km was applied to assign an average rainfall rate to each SSMIS footprint. This represents a compromise between the averaged 91-183 GHz channels (28 km) and the 19-37 GHz channels (38-73 km). For the high-resolution SNDB dataset, the half-power beamwidth was set to 13.5 km to match the effective footprint size of 13x14 km for these channels. Precipitation type was assigned to each SSMIS footprint using MERRA temperature profiles as follows:

- Snow if temperature at all levels (including skin) below 0°C,

- Rain if the coldest temperature within 500m of the surface is above 0°C

9

and skin, 2 m, and 10 m air temperature are above 0°C,

- Mix if neither of the above conditions are satisfied.

2.3. Retrieval Parameters

The iterative variational algorithm described in section 2 was used to retrieve temperature, water vapor, and non-precipitating cloud water at 15 atmospheric levels from 1000 hPa to 30 hPa, along with skin temperature, 10 m temperature, and emissivity in each channel. The a-priori covariance matrix for the atmospheric parameters (temperature, water vapor) was derived from 30 years (1981-2010) of MERRA reanalysis (Bosilovich, 2008) data independently at each MERRA grid point and for each month. As mentioned in section 2, this covariance matrix was orthogonalized and truncated so that the non-represented variability (defined as the sum of the magnitudes of the residual EOFs) did not exceed 3 K (temperature) or 1 g kg^{-1} (water vapor) at any individual atmospheric level, which is the minimum necessary to cause a significant (3 K) change in Tb in any SSMIS channel. The number of retained variables (out of a possible 32) is shown in Figure 1. Note that more atmospheric components are required in January compared to July due to the increased variability associated with strong temperature gradients in the cold season. There is also an effective reduction in atmospheric complexity over the high terrain of the southwest US, simply because MERRA levels are defined on constant pressure surfaces and fewer are available at high surface elevations.

Wind and cloud liquid water path (CLWP) are considered independent of the atmospheric temperature and water vapor state, and, like those variables, their mean and variance is derived from the MERRA reanalysis. The vertical profile of cloud water is considered a function of CLWP and interpolated from characteristic profiles at the 0.5, 2.5, 5, 15, 25, 50, 65, 85, 95, 97.5, and 99.5th percentiles of CLWP at each MERRA grid point for each month.

[Figure 1 about here.]

10

The surface emissivity is parameterized as a function of wind speed and skin temperature over water surfaces (assumed to be specular) using the FASTEM4 model (Liu et al., 2011). Although this model also accounts for wind direction and salinity, these are held constant since at frequencies used in this study, the resultant change in Tb is less than the assumed 3 K error. Over land surfaces (assumed to be Lambertian), emissivity means and covariance matrices are derived from the Tool to Estimate Land Surface Emissivity in the Microwaves (TELSEM; Aires et al. (2011)). As with the atmosphere, the emissivity covariance matrix is orthogonalized and the criteria for component retention is that remaining variability not exceed 0.01 in any channel. The resulting number of emissivity components (out of a possible 9) for the GMI configuration can be seen in Figure 1. Note the increased complexity of the surface in January relative to July over the Midwest and Plains due to the occasional presence of snow cover, which has highly variable microwave emissivity (Prigent et al., 2006).

2.4. Example Retrieval

An example case of the non-precipitation retrieval from a 2300 UTC overpass of F17 on 8 December 2009 is shown in Figure 2. At this time a large cyclone was developing over the central US. This storm deposited over 20 cm of snow over a band from western Kansas and Nebraska eastward to northern Illinois and southern Wisconsin, while at the same time brought widespread heavy rain to states further south and east, as shown in the composite reflectivity panel on the lower right.

The first column of Figure 2 depicts the cost function for the four different sensor configurations listed in Table 1 when MERRA and TELSEM climatology are used as the a-priori mean state ($\mathbf{x}_a$). Several differences between the sensors are apparent. All sensors capture the heavy rainfall over the Tennessee Valley quite well, although the GMI, SNDA, and SNDB configurations appear better capture the full extent of the light rain area. This is a result of the additional sensitivity to scattering in the 150 GHz channel relative to 91 GHz. In the mix and snow region, there is little apparent signal in the TMI retrieval.

11

The other sensors show a much higher cost function here, but this is generally indistinguishable from the large area of snow cover without precipitation falling over North Dakota and Montana. This is confirmed by the 150 GHz Tbs in this area, which show very cold values (<200K) indicative of low emissivity in this region. Because TELSEM was developed from SSM/I, TMI, and AMSU-A data (Aires et al., 2011), it extrapolates emissivities at 100 GHz to all higher frequencies. It is apparent from comparing the 89 and 150 GHz Tbs that in the North Dakota/Montana region, there is a significant difference in emissivity between these channels, leading to the large cost for all sensors that include the high-frequency channels.

False alarms, such as those caused by poor representation of the emissivity at high frequencies over snow covered surfaces in TELSEM, might be reduced by improving the characterization of the surface and atmosphere in $\mathbf{x}_a$ and $\mathbf{S}_a$ with ancillary data. One such source of data, represented in the second column of Figure 2, is the use of the reanalysis state provided by MERRA instead of the climatological mean in $\mathbf{x}_a$. There is a slight reduction in the cost function outside the precipitation regions; this reduction is more apparent in the sounding configurations owing to these channels' higher dependence on the atmospheric state than the window channels used by TMI and GMI.

Another source of data that could reduce the errors associated with snow cover is a real-time snow cover analysis coupled with a snow emissivity database. To create such a database, emissivities were calculated at all frequencies using the same retrieval described in section 2 (with zero a-priori covariance between channels) for FOVs with at least 1 cm of snow indicated by the Snow Data Assimilation System (SNODAS; Barrett (2003)) and no precipitation indicated by NMQ for the entire calendar year 2009. The mean and covariance matrices were then calculated and substituted for the TELSEM means and covariances in $\mathbf{x}_a$ and $\mathbf{S}_a$ when SNODAS indicated at least 1 cm of snow in the ground. These retrievals are shown in the third column of Figure 2. The use of this snow emissivity database results in is a large reduction in the cost function over much of the Dakotas in the GMI, SNDA, and SNDB retrievals. Some banding

12

features are now evident over eastern Nebraska, Iowa, and Minnesota. Note that large cost values remain just north of the US-Canada border where SNODAS data was unavailable and the unmodified TELSEM emissivities are used.

In the next section, the extent to which these ancillary datasets improve the overall skill of detecting precipitation will be evaluated for each sensor configuration over different surfaces, seasons, and types of precipitation.

[Figure 2 about here.]

3. Evaluation

The primary question this study seeks to address is: What is the minimum detectable precipitation rate that can be discerned from non-precipitating conditions by GPM-era passive microwave sensors? In this section we examine the results of the retrievals described in section 2 to establish this minimum threshold of detection, whether or not it improves (is reduced) when ancillary data are used as retrieval input, and how it changes with surface type, precipitation type, and sensor resolution.

3.1. Characteristics of Non-Precipitating Observations

The first step in this analysis is identifying the distribution of Φ associated with non-precipitating scenes. Under the assumption that $\mathbf{x}$ and $\mathbf{y}$ consist of independent standard normal random variables, the value of the cost function Φ (1) should follow a chi-squared distribution:

$$p(x,k) = \frac{x^{k/2-1}e^{-x/2}}{2^{k/2}\Gamma(k/2)} \tag{7}$$

with $k = m + n$ degrees of freedom, where m is the number of variables being retrieved and n is the number of observations. It can be inferred from Table 1 and Figure 1 that the degrees of freedom might range from around 10 (SNDB over ocean during summer) to 30 (GMI over snow during winter). To directly compare results from all retrievals, the cost function is normalized by $m + n$, which sets the theoretical expectation value to one for all $m + n$. The actual

13

distributions of Φ for non-precipitating and precipitating scenes are shown in Figure 3. The expectation value for all sensors is much lower than the theoretical value, an indication that there are effectively fewer degrees of freedom than $m+n$ in each retrieval. This may be the result of non-independence of some channels, insufficient information content in the observations to modify higher-order EOFs of the surface/atmosphere, and/or an overestimate of the observation error in $\mathbf{S}_y$. The latter was tested by reducing the diagonal elements of $\mathbf{S}_y$ to $(2 \text{ K})^2$ which resulted in an increase in non-convergence of non-precipitating cases. As far as precipitation detection is concerned, the overall distribution of Φ does not matter much so long as the Φ values in precipitating scenes are significantly higher than in non-precipitating scenes.

[Figure 3 about here.]

The sample case (Figure 2) shows significant variations in Φ over non-raining scenes, with high values over coasts and snow cover. If such high values are persistant over these surfaces, then the threshold of precipitation detection will likely be different among them as well. To illustrate the regional differences in the statistics of the distribution of Φ, the mean, standard deviation, and skewness of $\log_{10}(\Phi)$ for the GMI retrieval during the winter season are mapped in Figure 4. As expected, coasts stand out with significantly higher mean values (and logarithmic standard deviations) than all other areas. Values higher than 0 (which represent a normalized chi-squared expectation value of one) indicate that the surface emissivity climatology from TELSEM appears to insufficiently capture the surface variability in coastal areas. A closer examination indicates that the largest mean values of Φ occur just offshore, and are likely a consequence of the retrieval process. The retrieval uses TELSEM-derived emissivity EOFs if an SSMIS observation is flagged as a land, coast, or near coast surface type. Since TELSEM is only available over pixels that are predominately land at $0.25°$ resolution, the algorithm searches for the nearest valid TELSEM grid box, which is likely not representative in the near-coast case. An extension of TELSEM to 50km offshore would easily remedy this problem.

14

Aside from coasts, regions of snow cover in the upper Midwest and Rocky Mountains, as well as the Mississippi Delta region and the St. Lawrence River Valley and ocean surfaces show up as areas of slightly higher background Φ. Standard deviations are enhanced in the snow regions, particularly those on the southern edge of snow cover region in the Plains where snow cover is more episodic. The distributions of Φ also tend to be positively skewed in this area, indicating a long tail towards large Φ values relative to a symmetric lognormal distribution. Precipitation detection is made more difficult by a positively skewed distribution because the expected precipitation signal overlaps with this long tail, increasingly the false detection rate.

In order to account for these regional differences and to assist in drawing general conclusions about precipitation detectability over different surfaces, a combination of the SSMIS surface type flag (land, water, or coast) and SNODAS snow cover status is used to classify an observation as occurring over bare ground, snow covered ground, coast, or water. Thresholds of detection will be reported separately for each of these classes and sensor/ancillary data configuration.

[Figure 4 about here.]

3.2. Precipitation Detection Thresholds

The basis for the detection of precipitation by establishing a threshold value of Φ lies in the assumption that non-precipitating scenes will have relatively low values of Φ relative to precipitating scenes based on the formulation of $\mathbf{x}_a$ and $\mathbf{S}_a$. In the ideal case, the distributions of precipitating and non-precipitating Φ would have no overlap, and all precipitation would be detected by selecting a threshold value of Φ between the two distributions. In reality, there is some overlap between the distributions, and there must be a tradeoff between increasing the percentage of correct detections and minimizing misses. One way to optimize this tradeoff is to select a Φ threshold that maximizes the Heidke Skill Score (HSS; Wilks (2011)), which is a metric that measures the accuracy

15

of precipitation detection relative to random chance, at a given rainfall rate. A value of 1 indicates perfect detection of precipitation above some threshold R_0 and rejection of precipitation below R_0, 0 indicates no skill (the detected occurrence of precipitation is the same as the occurrence in the dataset, but with no correlation to observed precipitation) and negative values indicate a detection scheme that is less likely to correctly detect precipitation than random guess with the correct climatology frequency of precipitation. The HSS is defined as:

$$HSS = \frac{2(hc - fm)}{(h + m)(m + c) + (h + f)(f + c)} \tag{8}$$

where h, m, f, and c are the fractional hits, misses, false detections, and correct rejections in a contingency table. The HSS, therefore, can be considered a measure of the ability of Φ to differentiate between precipitation rates above and below any particular cutoff value.

The ability of each channel combination in Table 1 to detect various types of precipitation ranging from 0.5-2 mm hr^{-1} over the four surface classes is shown in Figure 5 as a function of month. The peak skill scores of the GMI, SNDA, and SNDB configurations exceed 0.5 over ocean and bare land surfaces for most of the year which is consistent with the MIRS algorithm (Iturbide-Sanchez et al., 2011), not surprising given its similar formulation to the retrieval used in this study. Over oceans, those sensors with the low-frequency channels (GMI and TMI) outperform the sounders (particularly SNDB) in detecting rain because the low-frequency channels are better-suited to sensing warm rain's emission signal over the low-emissivity ocean. Snow and mixed precipitation over water surfaces appear to be best detected by SNDB and SNDA, respectively, but there are relatively few occurrences of these events in the database.

[Figure 5 about here.]

Coastal regions have always been problematic for precipitation detection, and this is the case for our retrieval as well due to the uncertain land fraction, which itself may vary within the same set of observed Tbs due to the different channel beamwidths. Compounding this error in our retrieval is the apparent

16

poor representation of just-offshore regions in the TELSEM database (Figure 4). Nevertheless there is some ability for SNDB to detect precipitation there, particularly during the summer when the column water vapor is highest and the 89-183 GHz channels are least sensitive to the surface. Since these channels are available in the SNDA and GMI (minus the 183±1 GHz channel) configurations, retrievals from these instruments may be improved over coasts by assigning lower weights to the low-frequency and surface-sensitive channels.

Over bare ground, SNDA appears to be the best instrument for precipitation detection followed closely by GMI and SNDB with TMI in a distant fourth place. These rankings hold for all precipitation types although HSS values are distinctly lower for mixed precipitation and snow. There is a slight seasonality in the skill scores with a maximum in the summer. This is consistent with Iturbide-Sanchez et al. (2011) and has been attributed to the seasonal change in the relative contribution of easily-detected deep convection and weaker/shallower precipitation associated with synoptic-scale lifting mechanisms (Ebert et al., 2007).

Separating falling precipitation from snow on the ground is more challenging for reasons mentioned previously, primarily that the surface emission has a similar frequency dependence as precipitation. Therefore it is not surprising that the sounders have the highest skill. There is also a dependence on precipitation type, with rain and mixed precipitation being easier to detect over snow-covered surfaces than snowfall. Since the skill scores are calculated for the same precipitation rate, this is not a consequence of rain being more intense (on average) than snowfall. Instead, since TMI does not share in this trend, it may be concluded that the 150-183 GHz channels are more effective in discriminating precipitation from snow-covered surfaces in the higher water vapor content in the warmer environments associated with rain.

The skill scores presented in Figure 5 should be considered baseline values because no ancillary data such as atmospheric state and snow cover, which would be available in real time for GPM-era precipitation algorithms, were used. The impact of these data sources is discussed in section 3.3. Also, because there is

17

only a weak correlation between Φ and precipitation rate, it is difficult to use the HSS as a metric to identify the minimum detectable precipitation rate for each sensor/surface/phase combination. At the extremes, once could imagine a virga case (precipitation aloft that evaporates before reaching the ground) that produces a clear scattering signal, whereas an intense lake effect or upslope snow storm might be small and shallow enough so as to be indiscernible to the satellite. Indeed, when HSS is examined as function of precipitation rate (Figure 7), there is non-zero skill for the lightest (0.01 mm/hr) events and decreasing skill for very heavy events. The latter behavior simply indicates that at high precipitation rates, Φ itself is a poor proxy for intensity.

A more meaningful way to establish the minimum precipitation rate that can be detected invokes the signal-to-noise ratio. When the signal (precipitation) exceeds the noise (background variability) at a given value of Φ, the mean precipitation rate at that value of Φ can be thought of as the minimum detectable rate. While this does not explicitly take into account the climatological occurrence of precipitation as the HSS does, that fraction is low enough (around 15% in the NMQ dataset) that requiring 50% of retrievals in the Φ interval to be precipitating is indicative of the true ability of the sensor, not just chance occurrence.

This principle of detection is illustrated in Figure 6 for GMI retrievals of rain over bare ground. At low values of Φ (< 0.4), the occurrence of precipitation is lower than the dataset average, and tends to be very light (<0.1 mm hr^{-1}). As Φ increases so does the occurrence of precipitation and average precipitation rate. The 50% threshold is reached at a value of Φ of around 1, and at higher values of Φ, the precipitation fraction exceeds 95% giving very high confidence in the detection of higher rainfall rates (> 1.5 mm hr^{-1}). At the 50% detection threshold, the mean rainfall rate, including non-raining scenes, is about 0.4 mm hr^{-1}, thus the mean conditional rainfall rate is 0.8 mm hr^{-1}. Because of the positively-skewed distribution of rainfall rates, the conditional median is less than the conditional mean and tends to lie close to the overall mean.

[Figure 6 about here.]

Therefore, in Table 2, the rainfall detection threshold is indicated as the overall, or non-conditional (including zeros) mean rainfall rate, in the Φ interval for which rainfall occurrence is 50%. As with the HSS values in Figure 5, these values should be considered baseline since no real-time (as opposed to climatological) ancillary data was used. The percentage of total precipitation above the threshold Φ is also given. Values range from over 90% for rain over oceans to less than 10% for snow over snow cover and all precipitation over coastlines. For snow, these thresholds are generally consistent with the 0.5-1.2 mm hr^{-1} range found by Skofronick-Jackson et al. (2012) using model data. The over-ocean and coast statistics should be interpreted with caution, however, as a much smaller sample of precipitation over these surfaces was available, particularly for mixed precipitation and snow.

[Table 2 about here.]

All of the retrievals discussed in this section were performed on SSMIS observations averaged to half the native sampling both along- and cross-track, with the NMQ data convolved with a Gaussian weighting function of 38 km half-power width, which roughly matches the footprint of the lower-frequency channels on SSMIS. The high-frequency channels ($\geq$ 91 GHz) have a much smaller 13x14 km footprint, and to test the impact of this higher resolution on the results, the SNDB retrievals were performed again using this high-resolution dataset. For these data there is general broadening of the HSS curves (not shown) relative to their low-resolution equivalents, with increased skill at the light and heavy ends of the precipitation spectrum and a decrease at moderate rates. The main impact of increasing sensor resolution appears to be a more direct relationship between Φ and precipitation rate rather than an increase in the fraction of precipitation that is detected.

19

3.3. Impact of Ancillary Data

The a-priori atmosphere and surface state for the retrievals discussed in section 3.2 come from monthly climatology databases. Real-time forecasts or near-real time analyses of the atmospheric state are available from operational numerical weather prediction (NWP) centers. These should improve the skill of precipitation detection, particularly for the sounding instruments, by reducing the high Φ values associated with a highly anomalous atmospheric state, thereby reducing false detections. Similarly, a-priori knowledge of the presence of snow cover, which is also available from many sources in near-real-time, can be used to choose an appropriate surface emissivity database.

To test the impact of these ancillary datasets, the retrievals performed in section 3.2 were repeated with two modifications. First, the climatological atmospheric base state was replaced with the MERRA reanalysis valid at the time and location of each satellite observation. The atmospheric covariance remained the same as climatology, however. Second, when snow cover of greater than 1 cm was indicated by SNODAS, a snow emissivity database was used in place of TELSEM. This snow emissivity database was derived from the entire year (2009) of SSMIS observations when snow cover was present (again at the 1 cm threshold as indicated by SNODAS) under non-precipitating conditions, and analogous covariances and EOFs were derived.

[Figure 7 about here.]

The HSS from the retrievals that benefit from ancillary data are compared to the baseline HSS in Figure 7 for each surface type. To examine the causes of behavior of the HSS, two additional metrics, the probability of detection (POD) and false alarm rate (FAR) are also plotted in Figure 7. These are defined as:

$$POD = \frac{h}{h+m} \tag{9}$$

and

$$FAR = \frac{f}{f+c} \tag{10}$$

20

respectively.

As a function of rainfall rate, HSS tends to increase to a maximum near 1 mm hr^{-1} (except for coastal areas, where the maximum is nearer to 0.1 mm hr^{-1}). This increase corresponds to an increase in the POD, while the FAR remains relatively constant. The decrease in HSS at higher precipitation rates is a consequence of the lack of a direct relationship between Φ and R, which results in increasing false detections (light rainfall rates with high Φ) even though non-raining scenes are being correctly rejected and the miss rate decreases. This pattern remains the same when the ancillary data sources are introduced, but improvement in skill is clear in many of the retrievals.

Over ocean, the SNDA and SNDB retrievals benefit (via reduction of FAR) most from the use of reanalysis to set the atmosphere and surface (SST and wind are part of the ancillary dataset) state, whereas the instruments with dual-polarized window channels (TMI and GMI) do not benefit nearly as much. Even with reanalysis data, the SNDB retrieval does not perform as well as the others, perhaps due to insufficient sensitivity to warm rain due to the lack of low-frequency channels since the SNDA HSS is as high as TMI and GMI. Over coast, the only sensors with any meaningful skill (SNDA and SNDB) again benefit from a-priori knowledge of the atmospheric state. Over bare land, all sensors benefit from the reanalysis data to reduce the FAR but the improvement is smaller for those instruments with the most channels (GMI and SNDA), indicating that these appear to have sufficient information to retrieve the atmosphere and surface properties without the need for nudging from the reanalysis.

Over snow-covered surfaces, selection of the correct surface database results in a large improvement for all instruments, including the sounders, where it provides approximately the same increase in HSS as the use of MERRA data over the climatological base state. For the more surface-sensitive instruments (TMI and GMI), the improvement is even greater. One notable feature of the snow cover HSS statistics is that the highest skill clearly belongs to the SNDA configuration, pointing to the additional benefit of surface-insensitive channels near 50 GHz for detecting snow over snow-covered surfaces. As with the use

21

of the reanalysis state, these increases in skill primarily come about through reductions in the Far rather than an increase in POD.

The thresholds of detection are given in Table 3 for the ancillary data-aided retrievals. In all cases, the minimum threshold decreases and the volume of precipitation detected increases, and in some cases, a valid threshold exists where one did not without ancillary data. As suggested by the skill scores in Figure 7, the improvement is more marked for some sensor/surface combinations (e.g., sounder over ocean, GMI over snow) than others (e.g, GMI over ocean, SNDA over land). With ancillary data, the volume of precipitation detected is as high as 91% for GMI over ocean, but remains poor (generally under 50% and in some situations under 10%) for precipitation over coasts and snow cover. For comparison, the volume fraction of snowfall with NMQ reflectivity greater than 18 dBZ (roughly equivalent to the minimum thresholds of the Ku- and Ka-band on the GPM Dual-frequency Precipitation Radar) is 49%.

[Table 3 about here.]

4. Conclusion

This study presents an examination of the ability of GPM-era passive microwave sensors to delineate precipitation from non-precipitating scenes over the variety of surfaces and precipitation types that will be encountered in the 65°-inclination GPM core orbit. The basis for precipitation detection is a variational optimal estimation of non-precipitation parameters (atmospheric temperature and water vapor profiles, surface emissivity, and non-precipitating cloud water) which are represented as reduced-dimension EOFs in order to exploit covariance properties derived from climatology in order to constrain the retrieval. In this type of retrieval, a high cost function results when the scene being observed (precipitation) cannot be reconciled with any reasonable combination of the non-precipitating parameters.

Subsets of data from the SSMIS sensor on DMSP satellites F16 and F17 during 2009 were used to simulate the TMI, GMI, AMSU-A, and AMSU-B/MHS

22

microwave imagers and sounders which were matched with coincident ground radar reflectivity and precipitation rate from NMQ. The sensor with the best Heidke Skill Score was found to be GMI over ocean (90% of precipitation detected, with rates as low as 0.22 mm hr^{-1} having a 50% probability of detection) and the full sounder combination (AMSU-A+AMSU-B) over bare land (80% of precipitation detected, with rates as low as 0.26 mm hr^{-1} having a 50% probability of detection). Over snow-covered surfaces and coastlines, skill and the detected precipitation fraction were much lower although the sounders did show some skill in detecting precipitation over these surfaces. Increasing sensor resolution did not affect the fraction of precipitation detected although the minimum detectable rate increased slightly as a consequence of the shift in distribution of precpitation towards higher rates at higher resolutions.

In order to maximize the precipitation detection capability of each sensor, use of real-time ancillary data regarding the surface and atmospheric state is recommended, particularly for the sounding instruments over ocean where an increase in detected fraction of precipitation from 56% to 85% was noted. Although the reanalysis used in this study would not be availabel for real-time retrievals, numerical weather prediction models shoudl provide similar improvements relative to climatology. The use of a conditional snow cover emissivity dataset in place of an all-condition climatology greatly reduced the minimum detectable precipitation rate over snow-covered surfaces (from 0.89 mm hr^{-1} to 0.44 mm hr $^{-1}$) although the skill and detected fraction remain low compared to bare ground and ocean surfaces.

Many areas of improvements to the robustness of the ancillary data were noted. Real-time estimates of the atmospheric state covariance may be available from ensemble forecast systems which should more realistically constrain the temperature and water vapor profiles than the climatological covariance. Improvements to the TELSEM surface emissivity climatology, with separate snow and bare ground components and extension to at least 50 km offshore to better represent coastal regions, are recommended as well since these shortcomings were evident in the analysis of retrieval results.

23

In conclusion, the constellation of passive microwave sensors during the GPM era will offer the best opportunity yet afforded to sample the diverse characteristics of precipitation over most of the globe. However, intelligent use of ancillary data will be necessary in order to realize the full potential of these instruments. Even then, some regions, particularly coastlines and snow-covered surfaces, will remain challenges due to the fundamental difficulty of extracting a precipitation signal from the non-precipitating background variability. In these regions, a combination active sensors and future hyperspectral passive sensors will need to be relied upon to provide accurate precipitation estimates.

Acknowledgment

References

Aires, F., Prigent, C., Bernardo, F., Jimnez, C., Saunders, R., Brunel, P., 2011. A tool to estimate land-surface emissivities at microwave frequencies (telsem) for use in numerical weather prediction. Q.J.R. Meteorol. Soc. 137, 690–699.

Allison, L.J., Rodgers, E.B., Wilheit, T.T., Fett, R.W., 1974. Tropical cyclone rainfall as measured by the Nimbus Electrically Scanning Microwave Radiometer. Bull. Amer. Met. Soc. 55, 1074–1089.

Barrett, A., 2003. National Operational Hydrologic Remote Sensing Center Snow Data Assimilation System (SNODAS) Products at NSIDC. NSIDC Special Report 11. National Snow and Ice Data Center, Boulder, CO, USA.

Bauer, P., Moreau, E., Michele, S.D., 2005. Hydrometeor retrieval accuracy using microwave window and sounding channel observations. J. Appl. Meteor. 44, 10161032.

Bennartz, R., Bauer, P., 2003. Sensitivity of microwave radiances at 85-183 GHz to precipitating ice particles. Radio Sci. 38(4), 8075.

Bosilovich, M.G., 2008. NASA's modern era retrospective-analysis for research and applications: Integrating earth observations. Earthzine Available online at http://www.earthzine.org/2008/09/26/nasas-modern-era-retrospective-analysis/.

Boukabara, S.A., Garrett, K., Chen, W., Iturbide-Sanchez, F., Grassotti, C., Kongoli, C., Chen, R., Liu, Q., Yan, B., Weng, F., Ferraro, R., Kleespies, T., Meng, H., 2011. MiRS: An all-weather 1DVAR satellite data assimilation and retrieval system. IEEE Trans. Geosci. Remote Sensing 49, 3249 –3272.

Bytheway, J., Kummerow, C., 2010. A physically based screen for precipitation over complex surfaces using passive microwave observations. IEEE Trans. Geosci. Remote Sensing 48, 299 –313.

Chen, F., Staelin, D., 2003. AIRS/AMSU/HSB precipitation estimates. IEEE Trans. Geosci. Remote Sensing 41, 410 – 417.

Crum, T.D., Alberty, R.L., 1993. The WSR-88D and the WSR-88D operational support facility. Bull. Amer. Meteor. Soc. 74, 1669–1687.

Ebert, E.E., Janowiak, J.E., Kidd, C., 2007. Comparison of near-real-time precipitation estimates from satellite observations and numerical models. Bull. Amer. Meteor. Soc. 88, 4764.

Elsaesser, G., Kummerow, C., 2008. Towards a fully parametric retrieval of the non-raining parameters over the global oceans. J. Appl. Meteor. 47, 1599–1618.

Gloersen, P., Hardis, L., 1978. Scanning multichannel microwave radiometer (SMMR) experiment. In: Madris, C.R. (ed.) Nimbus 7 User?s Guide. NASA/GSFC, Greenbelt, MD.

Hewison, T., English, S., 1999. Airborne retrievals of snow and ice surface emissivity at millimeter wavelengths. IEEE Trans. Geosci. Remote Sensing 37, 1871 –1879.

Hollinger, J.P., Peirce, J.L., Poe, G.A., 1990. SSM/I instrument evaluation. IEEE Trans. Geosci. Remote Sensing 28, 781–790.

Iturbide-Sanchez, F., Boukabara, S.A., Chen, R., Garrett, K., Grassotti, C., Chen, W., Weng, F., 2011. Assessment of a variational inversion system for rainfall rate over land and water surfaces. IEEE Trans. Geosci. Remote Sensing 49, 3311 –3333.

Kim, M.J., 2006. Single scattering parameters of randomly oriented snow particles at microwave frequencies. J. Geophys. Res. 111, D14201.

Kim, M.J., Kulie, M.S., ODell, C., Bennartz, R., 2007. Scattering of ice particles at microwave frequencies: A physically based parameterization. J. Appl. Meteor. Climatol. 46, 615–633.

Kim, M.J., Weinman, J.A., Olson, W.S., Chang, D.E., Skofronick-Jackson, G., Wang, J.R., 2008. A physical model to estimate snowfall over land using AMSU-B observations. J. Geophys. Res. 113, D09201.

Kongoli, C., Pellegrino, P., Ferraro, R.R., Grody, N.C., Meng, H., 2003. A new snowfall detection algorithm over land using measurements from the advanced microwave sounding unit (AMSU). Geophys. Res. Lett. 30(14), 1756.

Kummerow, C., Hong, Y., Olson, W.S., Yang, S., Adler, R.F., McCollum, J., Ferraro, R., Petty, G., Shin, D.B., Wilheit, T.T., 2001. The evaluation of the Goddard Profiling Algorithm (GPROF) for rainfall estimation from passive microwave sensors. J. Appl. Meteor. 40, 1801–1820.

Kummerow, C., Weinman, J.A., 1988. Determining microwave brightness temperatures from precipitating horizontally finite and vertically structured clouds. J. Geophys. Res. 93, 3720–3728.

Kummerow, C.D., Ringerud, S., Crook, J., Randel, D., Berg, W., 2011. An observationally generated a-priori database for microwave rainfall retrievals. J. Atmos. Oceanic Technol. 28, 113–130.

Kunkee, D., Swadley, S., Poe, G., Hong, Y., Werner, M., 2008. Special Sensor Microwave Imager Sounder (SSMIS) radiometric calibration anomalies Part I: Identification and characterization. IEEE Trans. Geosci. Remote Sensing 46, 1017 –1033.

Liu, G., 2004. Approximation of single scattering properties of ice and snow particles for high microwave frequencies. J. Atmos. Sci. 61, 24412456.

Liu, G., Curry, J., 1997. Precipitation characteristics in Greenland-Iceland-Norwegian Seas determined using satellite microwave data. J. Geophys Res. 102, 13987–13997.

Liu, Q., Weng, F., English, S., 2011. An improved fast microwave water emissivity model. IEEE Trans. Geosci. Remote Sensing 49, 1238 –1250.

Maddox, R.A., Zhang, J., Gourley, J.J., Howard, K.W., 2002. Weather radar coverage over the contiguous United States. Wea. Forecasting 17, 927934.

Noh, Y.J., Liu, G., Jones, A.S., Haar, T.H.V., 2009. Toward snowfall retrieval over land by combining satellite and in situ measurements. J. Geophys. Res. 114, D24205.

Noh, Y.J., Liu, G., Seo, E.K., Wang, J.R., Aonashi, K., 2006. Development of a snowfall retrieval algorithm at high microwave frequencies. J. Geophys. Res. 111, D22216.

Petty, G.W., Huang, W., 2010. Microwave backscatter and extinction by soft ice spheres and complex snow aggregates. J. Atmos. Sci. 67, 769–787.

Prabhakara, C., Short, D.A., Wiscombe, W., Fraser, R.S., Vollmer, B.E., 1986. Rainfall over oceans inferred from Nimbus 7 SMMR: Application to 1982-83 el ni no. J. Climate Appl. Meteor. 25, 1464–1474.

Prigent, C., Aires, F., Rossow, W.B., 2006. Land surface microwave emissivities over the globe for a decade. Bull. Am. Meteorol. Soc. 87, 15731584.

Rodgers, C.D., 2000. Inverse Methods for Atmospheric Sounding: Theory and Practice. World Scientific Publishing Co., Singapore.

Rosenkrantz, P.W., 1998. Water vapor microwave continuum absoption: A comparison of measurements and models. Radio Sci. 33, 919–928.

Rosenkrantz, P.W., 1999. Correction to "water vapor microwave continuum absoption: A comparison of measurements and models". Radio Sci. 34, 1025.

Sapiano, M.R.P., Berg, W.K., McKague, D.S., Kummerow, C.D., 2012. Toward an intercalibrated fundamental climate data record of the SSM/I sensors. IEEE Trans. Geosci. Rem. Sens. , in press.

Skofronick-Jackson, G., Johnson, B.T., 2011. Surface and atmospheric contributions to passive microwave brightness temperatures for falling snow events. J. Geophys. Res. 116, D02213.

Skofronick-Jackson, G., Johnson, B.T., Munchak, S.J., 2012. Detection thresholds of falling snow from satellite-borne active and passive sensors. IEEE Trans. Geosci. Remote Sensing , submitted.

Skofronick-Jackson, G., Kim, M.J., Weinman, J., Chang, D.E., 2004. A physical model to determine snowfall over land by microwave radiometry. IEEE Trans. Geosci. Remote Sensing 42, 1047 – 1058.

Spencer, R.W., 1986. A satellite passive 37-GHz scattering-based method for measuring oceanic rain rates. J. Climate Appl. Meteor. 25, 754–766.

Surussavadee, C., Staelin, D., 2009. Satellite retrievals of arctic and equatorial rain and snowfall rates using millimeter wavelengths. IEEE Trans. Geosci. Remote Sensing 47, 3697 –3707.

Tretyakov, M., Parshin, V., Koshelev, M., Shanin, V., Myasnikova, S., Krupnov, A., 2003. Studies of 183-GHz water line: broadening and shifting by air, N2 and O2 and integral intensity measurements. J. Molecular Spectroscopy 218, 239 – 245.

Weng, F., Yan, B., Grody, N.C., 2001. A microwave land emissivity model. J. Geophys. Res. 106, 20115–20123.

Wilheit, T.T., Chang, A.T.C., V. Rao, M.S., Rodgers, E.B., Theon, J.S., 1977. A satellite technique for quantitatively mapping rainfall rates over the oceans. J. Appl. Meteor. 16, 551–560.

Wilks, D.S., 2011. Statistical Methods in the Atmospheric Sciences. Elsevier.

Wu, R., Weinman, J.A., 1984. Microwave radiances from precipitating clouds containing aspherical ice, combined phase, and liquid hydrometeors. J. Geophys. Res. 89, 7170–7178.

Yan, B., Weng, F., 2008. Intercalibration between special sensor microwave imager/sounder and special sensor microwave imager. IEEE Trans. Geosci. Remote Sensing 46, 984 –995.

Zhang, J., Howard, K., Langston, C., Vasiloff, S., Kaney, B., Arthur, A., Cooten, S.V., Kelleher, K., Kitzmiller, D., Ding, F., Seo, D.J., Wells, E., Dempsey, C., 2011. National mosaic and multi-sensor QPE (NMQ) system: Description, results, and future plans. Bull. Amer. Meteor. Soc. 92, 1321–1338.

List of Figures

Figure 1: Number of atmosphere (a,c) and surface (b,d) EOFs retrieved in January (a,b) and July (c,d) based on MERRA (atmosphere) and TELSEM (surface) climatology for the simulated GMI sensor, which has 10 channels at 9 center frequencies/polarization combinations.

31

Figure 2: Cost function for different sensor configurations (rows) and ancillary data (columns) as applied to SSMIS data from 2200 UTC 8 December 2009. For reference, the 91H and 150 H SSMIS Tbs are shown in the upper right along with the concurrent SNODAS snow depth analysis and NMQ composite reflectivity in the lower right.
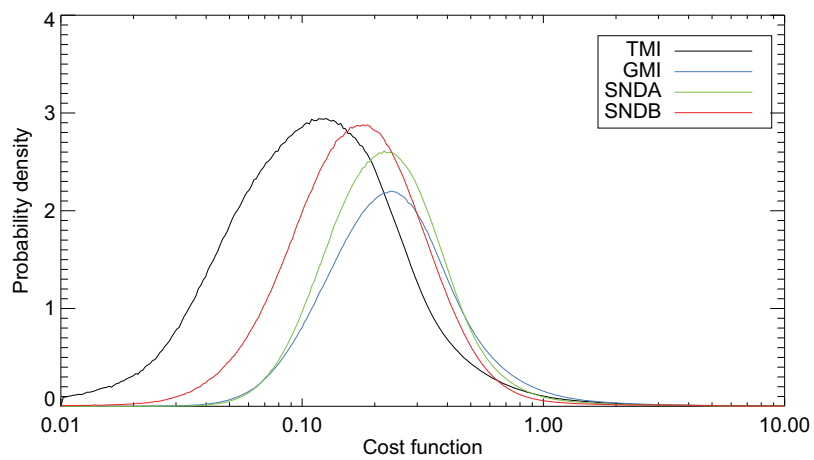
Figure 3: Histograms of Φ for non-raining scenes for all sensor configurations for the year 2009 over CONUS. The histograms have been normalized such that the area under each curve is equal to one.
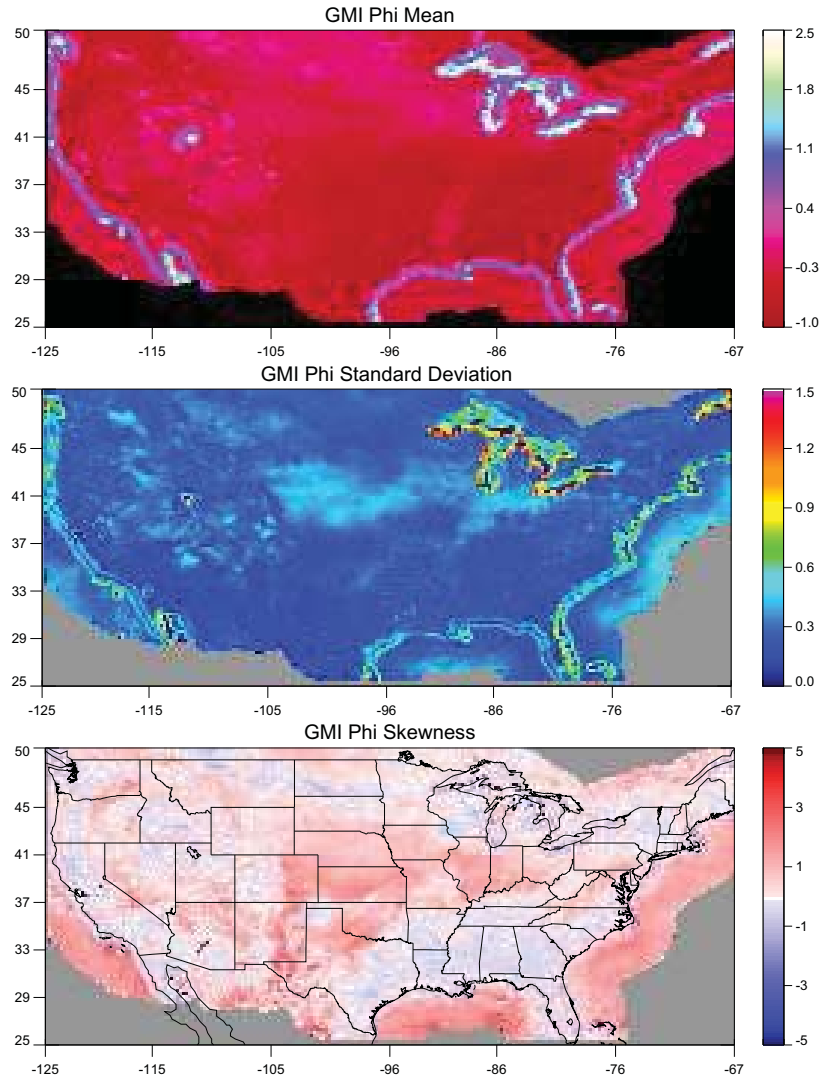
Figure 4: Statistics of the distribution of non-precipitating Φ values gridded at $0.25°$ resolution. All statistics were performed on the base-10 logarithm of Φ to be consistent with the apparent lognormal distribution of Φ in Figure 3.
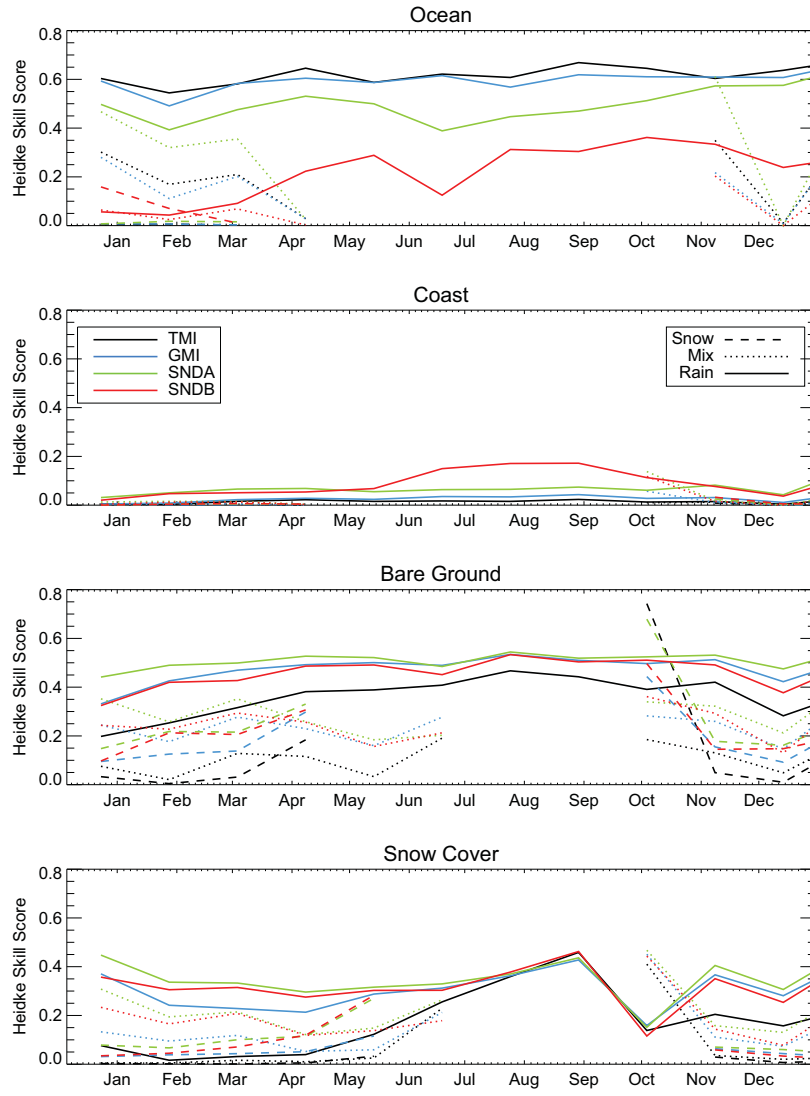
Figure 5: Time series of monthly Heidke Skill Score for each sensor, surface, and precipitation type for precipitation rates between 0.5 and 2 mm hr^{-1}.
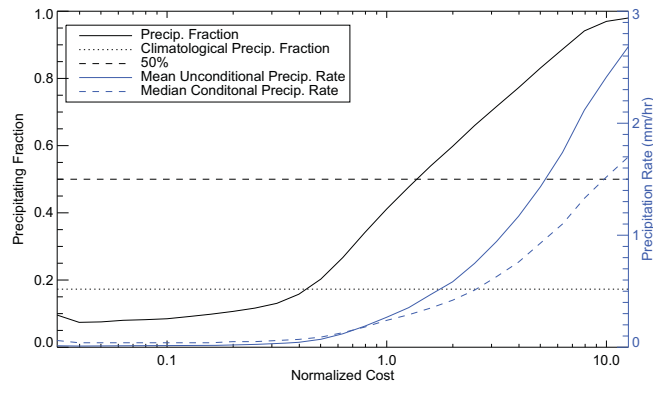
Figure 6: Fractional occurrence of rain and mean/median rainfall rate as a function of normalized retrieval cost (Φ) for the baseline GMI retrieval over bare land surfaces. The climatological precipitation fraction and 50% threshold are indicated by the dotted and dashed lines, respectively.
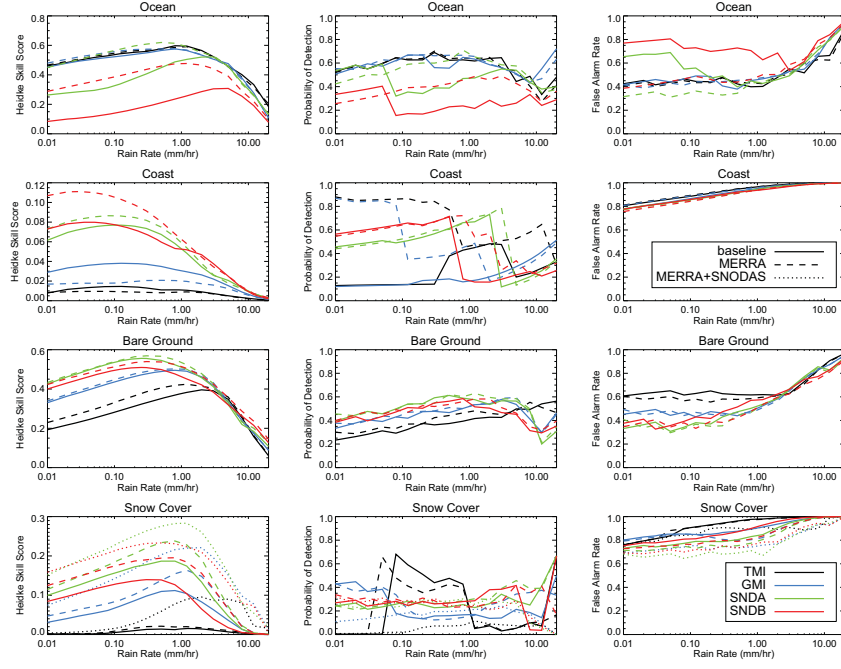
Figure 7: Maximum Heidke Skill Score (HSS; left), Probability of Detection (POD; middle), and False Alarm Rate (FAR; right) as a function of precipitation rate for each sensor and surface type for all months. The POD and FAR are calculated at the same Φ threshold that maximizes HSS. The ancillary data-augmented retrievals are indicated by the dashed (MERRA reanalysis) and dotted (MERRA reanalysis and SNODAS snow cover) lines. Note that the vertical scale is different for each plot to emphasize the changes that result from the use of ancillary data.

List of Tables

Table 1: List of SSMIS channel frequencies (GHz) and polarizations that are used to mimic each sensor configuration explored in this section (TMI=TRMM Microwave Imager/AMSR, GMI = GPM Microwave Imager, SNDA = AMSU-A+AMSU-B/MHS, SNDB = AMSU-B/MHS). Channels not available on SSMIS are crossed through. Note that the 50-53 GHz channels on F16 are vertically polarized while those on F17 are horizontally polarized.

SSMIS	TMI	GMI	SNDA	SNDB
	~~10H~~	~~10H~~		
	~~10V~~	~~10V~~		
19H	19H	19H		
19V	19V	19V		
22V	21V	23V	23V	
37H	37H	37H		
37V	37V	37V	31V	
50V/H			50V	
52V/H			52V	
53V/H			53H	
91H	85H	89H		
91V	85V	89V	89	89
150H		166H	150/157	150/157
		~~166V~~		
183±6		183±7	183±7	183±7
183±3		183±3	183±3	183±3
183±1			183±1	183±1

Table 2: Minimum detectable precipitation rate (mm hr $^{-1}$) and percentage of precipitation volume detected (in parentheses) for each sensor, surface type, and precipitation type in the baseline configuration. The minimum detectable rate is defined as the mean rainfall rate at the lowest Φ value where at least 50% of retrievals have $R \geq 0.01$mm hr^{-1}. Therefore, these values should be doubled to represent the conditional mean precipitation rate in that interval. Cells are left blank if no such value exists.

Surface	Phase	TMI	GMI	SNDA	SNDB
Ocean	All	0.23(88%)	0.28(87%)	0.97(56%)	2.22(18%)
	Snow	—	—	—	—
	Mix	1.06 (4%)		0.53(46%)	—
	Rain	0.19(91%)	0.23(89%)	0.91(58%)	2.12(20%)
Coast	All	—	—	1.19 (2%)	—
	Snow	—	—	—	—
	Mix	—	—	—	—
	Rain	—	—	1.29 (2%)	—
Bare	All	1.11(42%)	0.40(68%)	0.26(80%)	0.28(75%)
Land	Snow	—	0.56 (5%)	0.24(36%)	0.25(30%)
	Mix	—	0.44(29%)	0.26(53%)	0.23(48%)
	Rain	0.99(47%)	0.40(73%)	0.26(81%)	0.28(77%)
Snow	All	—	0.86 (3%)	0.89 (4%)	—
Cover	Snow	—	—	0.89 (1%)	—
	Mix	—	0.81 (2%)	0.63(19%)	0.77 (9%)
	Rain	—	0.43(35%)	0.25(60%)	0.22(59%)

Table 3: Same as Table 2, except that MERRA atmospheric state was substituted for climatology as the a-priori atmospheric state and, for snow covered surfaces, a snow cover emissivity database was substituted for TELSEM.

Surface	Phase	TMI	GMI	SNDA	SNDB
Ocean	All	0.22(89%)	0.22(90%)	0.25(85%)	0.63(61%)
	Snow	—	—	—	—
	Mix	0.85 (4%)		0.50(49%)	0.44(12%)
	Rain	0.18(91%)	0.17(91%)	0.24(81%)	0.47(65%)
Coast	All	—	2.11(8%)	0.74(12%)	—
	Snow	—	—	—	—
	Mix	—	—	0.96(13%)	0.81(9%)
	Rain	—	—	0.58(42%)	0.41(59%)
Bare	All	0.77(56%)	0.39(71%)	0.26(81%)	0.28(78%)
Land	Snow	1.32 (1%)	0.50(10%)	0.25(38%)	0.25(36%)
	Mix	1.83 (2%)	0.44(29%)	0.22(58%)	0.24(57%)
	Rain	0.69(61%)	0.38(73%)	0.26(82%)	0.28(79%)
Snow	All	1.41 (1%)	0.56(13%)	0.44(23%)	0.53(15%)
Cover	Snow	—	0.66 (1%)	0.60 (4%)	0.60 (1%)
	Mix	1.03 (0%)	0.60(14%)	0.39(42%)	0.46(37%)
	Rain	0.91(13%)	0.30(55%)	0.22(65%)	0.22(66%)